Cyclic cold isostatic pressing and improved particle packing of coarse grained oxide ceramics for refractory applications

Stefan Schafföner[a,b,*], Jens Fruhstorfer[b], Susann Ludwig[b], Christos G. Aneziris[b]

[a]*Department of Materials Science and Engineering, Norwegian University of Science and Technology, 7491 Trondheim, Norway*
[b]*Institute of Ceramic, Glass and Construction Materials, TU Bergakademie Freiberg, Agricolastrasse 17, 09599 Freiberg, Germany*

Abstract

This study investigated the cold isostatic pressing of coarse grained alumina refractories applying either a cyclic pressure increase or a cycling at maximum pressure. Additionally the effects of the maximum pressure and the particle size distribution on physical, mechanical and thermomechanical properties were analyzed. The cyclic pressure increase resulted in a slightly higher apparent density and lower apparent porosity. A cycling at maximum pressure decreased the median pore size to some extent. Remarkably, an optimized particle size distribution resulted in a lower apparent porosity, lower median pore size and in a higher Young's modulus before and after thermal shock together with a slightly lower relative decrease of the Young's modulus. A higher pressing pressure which decreased the apparent porosity did not affect the Young's modulus. Thus, apparently the optimized particle size distribution improved the particle packing which was associated with a smaller median pore size. This smaller pore size increased the number of pores relative to the total porosity, which then acted as points of crack initiation and crack deflection limiting the length of propagating cracks in case of thermal shock. Thus, tailoring the pore size distribution is a promising starting point to improve the thermomechanical properties of refractories.

Keywords: Cold isostatic pressing, Refractories, Particle size distribution, Thermal shock resistance

1. Introduction

Cold isostatic pressing (CIP) is one of the best-known forming techniques to produce ceramic products with high length to diameter ratios or complicated shapes [1–5]. During cold isostatic pressing according to the wet bag process, powders or granules are filled into an elastic mold, which is later often vacuum sealed. The filled elastic mold is then placed in a fluid and by applying a high pressure on the fluid a very homogeneous compaction of the ceramic body can be achieved [6]. The advantages of cold isostatic pressing compared to uniaxial pressing are much lower density gradients and thus a higher mechanical reliability of the ceramic products [7, 8].

Several authors studied the cyclic uniaxial and cyclic isostatic compaction of ceramic, metal and composite powders. Especially a cycling at maximum pressure resulted in smaller density gradients and a stronger densification [9–17].

For single phase powders a considerable higher densification was observed with cyclic pressing, which was explained by an improved particle packing accompanied with a higher particle coordination number and by the fracture of agglomerates [9, 14, 18, 19]. For composites an even higher relative improvement in densification was attributed to the volumetric mismatch between the different phases during a pressure change [11, 14, 17, 20, 21]

In general cyclic cold isostatic pressing was only investigated for fine grained ceramics. However, cyclic cold isostatic pressing of coarse grained oxide ceramics such as refractories still remains unstudied.

Thus, the purpose of this study is to describe and examine the effects and possible benefits of cyclic cold isostatic pressing of coarse grained oxide ceramics for refractory applications. Investigated experimental factors were the maximum pressure, the pressure amplitude and the particle size distribution. Furthermore, the difference between a cyclic and linear pressure increase was determined.

*Corresponding author
Email address: schaffoener@gmail.com (Stefan Schafföner)

2. Experimental

2.1. Materials

The present study investigated the cold isostatic pressing of coarse grained ceramics using alumina as a common refractory raw material. All experiments were performed using full factorial experimental designs.

In all experiments tabular alumina (T60/T64, Almatis GmbH, Germany) was used because it is a widely available raw material [22]. In order to evaluate the effect of the particle size distribution on the cold isostatic pressing, two compositions were designed according to a recently proposed particle size model, which is given in equation (1) [23]:

$$\mathrm{CPFT} = \left(\frac{\mathrm{d}}{\mathrm{d_{max}}}\right)^{\left(\mathrm{n_{min}} + \mathrm{d}\cdot\frac{\mathrm{n_{max}}-\mathrm{n_{min}}}{\mathrm{d_{max}}}\right)} \quad (1)$$

where CPFT is the cumulative percentage of particles finer than a particle diameter d, $\mathrm{d_{max}}$ is the maximum particle diameter of the particle size distribution, $\mathrm{n_{max}}$ is the distribution modulus at $\mathrm{d_{max}}$, whereas $\mathrm{n_{min}}$ is the distribution modulus of an infinitesimal particle size.

The particle size distribution was included as the first factor (A) in the factorial experimental design. The maximum particle size for all particle size distributions was held constant at $\mathrm{d_{max}} = 3\,\mathrm{mm}$. The particle size distribution was varied by changing the parameter $\mathrm{n_{min}}$ according to equation (1) on two levels. The parameter $\mathrm{n_{max}}$ was held constant at 0.8. The factorial experimental design is summarized in Table 1, whereas the specific composition for each designed particle size distribution is summarized in Table 2.

For all experiments a wax dispersion was applied as a binder (Zusoplast WE 52, Zschimmer & Schwarz GmbH & Co. KG, Germany) because it was previously successfully used to optimize a batch composition for uniaxially die pressed alumina-mullite refractories [24]. The batches were prepared by ordered mixing using a conventional mortar mixer (ToniMIX, Toni Technik Baustoffprüfsysteme GmbH, Germany) [22, 24]. In this ordered mixing procedure the coarse grained particle fractions (> 0.5 mm) were first dry mixed for 4 min before the binder was added and stirred for another 4 min. Finally the fine particle fractions were added and the whole mixture was stirred twice for 4 min. Between each step the mixing container was carefully scrapped to ensure a homogeneous mixture. The dry mass of each batch was 3 kg.

The binder amount was optimized for each particle size distribution similar to Schafföner et al. [25]. For this purpose samples with three different binder amounts were uniaxially pressed (ES 270, RUCKS Maschinenbau GmbH, Germany) with a pressure of 120 MPa, see Table 3. The samples were then dried at 80 °C and 110 °C for 6 h at both temperatures before they were fired in air atmosphere with a heating rate of 2 K/min, a maximum temperature of 1650 °C and a dwell time of 4 h. Subsequently, the fired samples were investigated on their apparent porosity and apparent density according to the standard DIN EN 993-1 using water as the immersion fluid. The compositions of each particle size distribution resulting in a low apparent porosity together with an even surface were later used for the cold isostatic pressing experiments.

2.2. Cyclic cold isostatic pressing

The samples were pressed in a newly developed cold isostatic press (EPSI N.V., Belgium) with an inner height of 1 m and an inner diameter of 0.25 m which allows a pressure cycling. The used cylindrical molds made of EPDM rubber with a Shore hardness of 40A had an inner effective height of 63 mm after inserting a rubber cap and an inner diameter of 62 mm. To minimize the entrapped air, the filled molds were evacuated for 10 min before pressing.

As a second factor in the factorial experimental design the maximum pressure (B) was varied between 75 MPa (−1, lower level) and 120 MPa (+1, higher level).

To determine the effect of the cyclic cold isostatic pressing, the cycling during the pressure increase (C) and at the maximum pressure (D) were evaluated as two different factors in the factorial experimental design.

At the lower level of the factor C the pressure was linearly increased to the maximum pressure with 1 MPa/s. At the higher level, however, the pressure was cycled during the pressure increase. For a maximum pressure of 75 MPa the pressure was cycled five times during the pressure increase, while for a maximum pressure of 120 MPa the pressure was cycled nine times.

At the lower level of the factor D the pressure was again held constant at the maximum pressure, whereas at the higher level the pressure was cycled for ten times with an amplitude of 25 MPa. The resulting pressure procedures are given in Figs. 1 and 2.

The order of the pressing procedures was random, whereas during each pressure cycle four samples of one of the two compositions were prepared. The order of the two compositions was again randomly chosen for each run of the experimental design.

Table 1: Factors of the 2^4 full factorial experimental design. The thermal shock test was included as factor E in the statistical analysis where appropriate resulting in a 2^5 experimental design.

Factor	Identifier	Lower level (-1)	Higher level (+1)
Particle size distribution	A	n_{min} = 0.27 ($Batch_1$)	n_{min} = 0.4 ($Batch_2$)
Maximum pressure	B	75 MPa	120 MPa
Pressure increase	C	linear	cycled
Maximum pressure cycling	D	no (constant)	yes (cycled)
Thermal shock	E	without	with

Table 2: Compositions of the different investigated batches after optimizing the binder amount (see Table 3).

Product Name	Raw Material	Grain size fraction	$Batch_1$ (n_{min} = 0.27)	$Batch_2$ (n_{min} = 0.4)
Almatis T 60/64	Al_2O_3	1 – 3 mm	40 wt.%	45 wt.%
		0.5 – 1 mm	5 wt.%	10 wt.%
		0 – 0.5 mm	10 wt.%	10 wt.%
		0 – 0.2 mm	20 wt.%	30 wt.%
		0 – 0.02 mm	25 wt.%	5 wt.%
Zusoplast WE 52	PVA binder	mass relative to dry mass	2.50 wt.%	2.50 wt.%

Table 3: Experimental design and results to optimize the binder content of each batch

Run		1	2	3	4	5	6
Factor A	Distribution modulus n_{min}	0.27	0.27	0.27	0.4	0.4	0.4
Factor B	Actual binder content	1.51 wt.%	2.00 wt.%	2.51 wt.%	1.53 wt.%	2.00 wt.%	2.50 wt.%
Apparent porosity	(%)	17.66	18.01	17.81	19.13	19.24	19.03
Apparent density	(g/cm^3)	3.11	3.09	3.10	3.02	3.02	3.03
Sinter diameter change	(%)	−0.41	−0.41	−0.41	−0.30	−0.30	−0.30

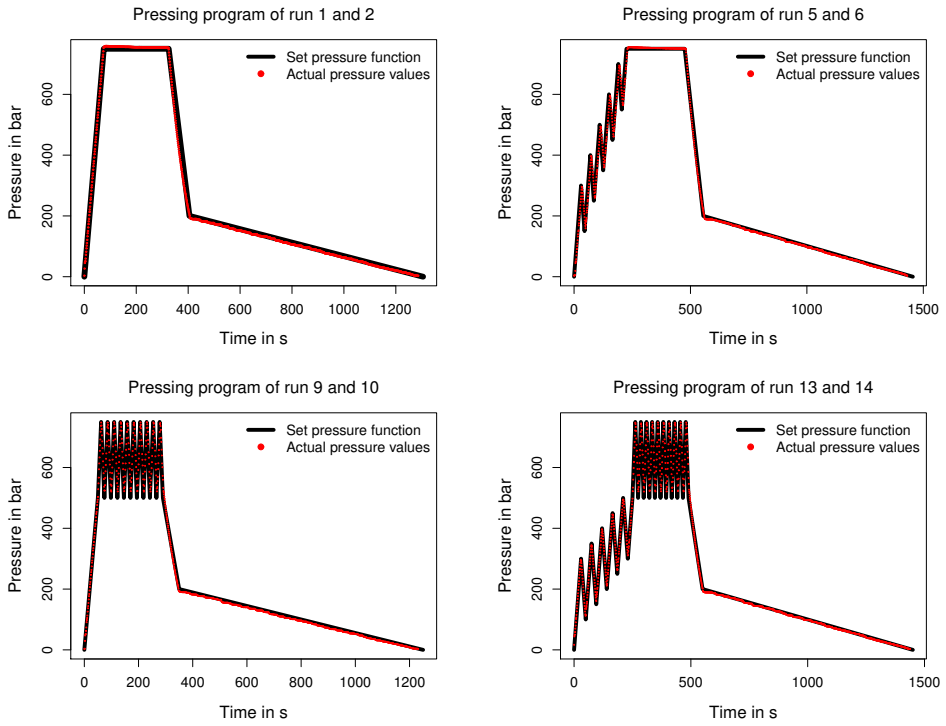

Figure 1: The plots present the set pressure together with the measured pressure values as a function of the time for the programs with a maximum pressure of 75 MPa. For each pressing program only one of the two pressure cycles is given to improve the illustration. For all pressing programs an excellent agreement of the set pressure function and the measured was obtained.

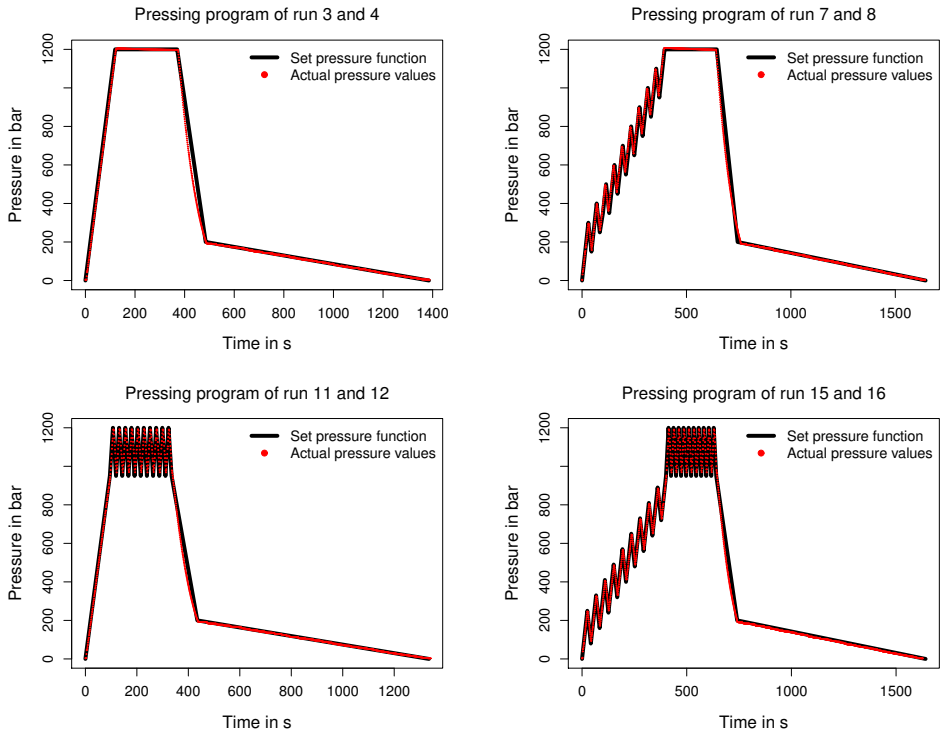

Figure 2: The pressing programs with a maximum pressure of 120 MPa also showed an excellent agreement of the set and measured pressure function.

2.3. Characterization of physical, mechanical and thermomechanical properties

The isostatically pressed samples were dried and fired as the uniaxially pressed ones for the batch optimization. After firing the samples were first examined regarding their apparent porosity and apparent density according to the standard DIN EN 993-1.

Later on, the samples were again dried and a single block with a size of about 20 mm × 20 mm × 20 mm from each batch was cut form the center of the samples using a diamond saw. The cutting ensured an identical sampling for each batch. The cut out blocks were then crushed. Later on, the crushed material was used to determine the pore size distribution using mercury porosimetry (Autopore V 9600, Micrometrics GmbH, Germany) according to the standard DIN 66133.

Furthermore, the thermal shock resistance was evaluated using again a single cylinder of each batch (factor E in the statistical analysis). The thermal shock resistance was determined similar to the standard DIN EN 993-11 using pressurized air. In contrast to the standard, cylinders were used instead of bars. The thermal shock resistance was evaluated by comparing the dynamic Young's modulus before and after a single thermal shock.

The Young's modulus was calculated according to the standard DIN EN 843-2 measuring the velocity of sound. For the calculation of the Young's modulus a Poisson ratio of 0.2 was assumed for alumina, which is consistent with Asmani et al. [26].

2.4. Statistical analysis

To determine the significance of the investigated factors, the full factorial experimental design was evaluated with analysis of variance (ANOVA) and by applying Lenth's pseudo-standard error (PSE) [27]. ANOVA is the extension of the Student's t-test for more than one variable or if a single variable has more than two levels [25, 28, 29]. For the ANOVA the fourth-order and third-order interactions were generally not taken into account in order to obtain a sufficient number of degrees of freedom. This is necessary to estimate an error term for the ANOVA [30, 31].

Meanwhile, the pseudo-standard error is used to construct Lenth plots, which are very effective to present the effects of factorial experiments with a single replication. Furthermore, in Lenth plots active and inactive effects can be easily identified. Thereby active means statistically significant, while inactive means statistically insignificant [27, 32].

Both applied methods to analyze the factorial experimental design assume effect hierarchy and effect sparsity. Effect hierarchy assumes that main and low order interactions are more likely to be statistically significant than higher order interactions. Effect sparsity, on the other hand, assumes that only a small number of effects are active, while the majority of the effects is inactive [27, 30, 33]. Furthermore, by applying two methods to analyze the full factorial experiment, an inappropriate pooling of error mean squares of higher-order interactions can be avoided. Thus, the negligence of possibly active higher order interactions becomes less probable. All statistical analyses were performed using the software package R [34].

3. Results and discussion

In this study the cyclic cold isostatic pressing of coarse grained ceramics for refractory applications was investigated in a full factorial experimental design. The present section will first describe the optimization of the used batches and cold isostatic pressing programs. Then follows an evaluation of the resulting physical, mechanical and thermomechanical properties. All measured properties are summarized in Table 4.

3.1. Batch optimization and cyclic cold isostatic pressing

To optimize the batch compositions, samples with three different binder amounts were uniaxially pressed for each particle size distribution. Results in Table 2 show that a higher distribution modulus n_{min} yielded a composition with a much lower content of the finest particle fractions. Meanwhile, as can be seen from the results in Table 3 the samples with a lower distribution modulus n_{min} resulted in a significantly lower apparent porosity. As a consequence the lower apparent porosity also resulted in a higher apparent density.

The reason for the lower apparent porosity and higher apparent density of the batches with a lower distribution modulus n_{min} was most likely a better particle packing. Even so, it has to be noted that the apparent density is not only affected by the apparent porosity but also by the batch composition because the apparent density of tabular alumina raw materials generally decreases with a larger particle size [23, 35].

For both compositions, the samples with the medium amount of binder (run 2 and 5, respectively) resulted in the highest apparent porosity. The batches with the highest amount of binder (2.5 wt.%, run 3 and 6, respectively) were chosen for further experiments because these batches had a low apparent porosity as well as the best surfaces after pressing. The optimized compositions are henceforth referred to as $Batch_1$ and $Batch_2$, which are given in Table 2.

Figs. 1 and 2 present the set pressing programs together with the measured pressure values. Remarkably, a very high agreement of the set and measured pressure values was obtained for all pressing programs. Only for the programs with a cycling at maximum pressure (level +1, factor D) and to a smaller extent for the cycling at increasing pressure (level +1, factor C) the minimum pressure during a pressure cycle was not entirely reached. However, it should be noted that this difference between the set and actually obtained pressure values during cycling was very low in relative terms.

3.2. Sintering shrinkage

The linear sintering shrinkage for all batches given in Table 4 was below 1 % and thus to some extent lower than recently reported linear shrinkage values for tabular alumina refractories [22]. The somewhat lower sintering shrinkage might be the consequence of a lower firing temperature in the present study.

Inspection of the Lenth plot in Fig. 3 indicates that the particle size distribution (A) and the interaction of the pressure cycling factors (CD) were possibly significant regarding the sintering shrinkage, which was consistent with the ANOVA in Table 5.

The higher sintering shrinkage at a lower distribution modulus n_{min} (factor A, level −1) can be attributed to the higher level of the finest particle fraction. The higher amount of finest grains then led to a higher sintering effect, while the coarser grain size fractions antagonized the sintering shrinkage [36, 37].

Meanwhile only the interaction CD was statistically significant, whereas their respective main effects C and D were not. As detailed in the interaction plot in Fig. 4, low sintering diameter changes of −0.22 % and −0.08 % were obtained when both factors were either at their low or high level. A combination of a high level of C or D and with a low level of the other factor, on the other hand, resulted in high sintering diameter changes of −0.44 % and −0.50 %, respectively. Future studies should investigate whether this interaction is reproducible because the observed effect was relatively small.

3.3. Apparent density and porosity

According to the Lenth plots in Figs. 5 and 6 in conjunction with the results from the ANOVA in Table 5, the particle size distribution (A) as well as the maximum pressure (B) had a significant effect on the apparent porosity and apparent density, respectively. Furthermore, the ANOVA in Table 5 also indicates a significant effect of a cycled pressure increase (C) and of the interaction AB. As expected, all significant effects were

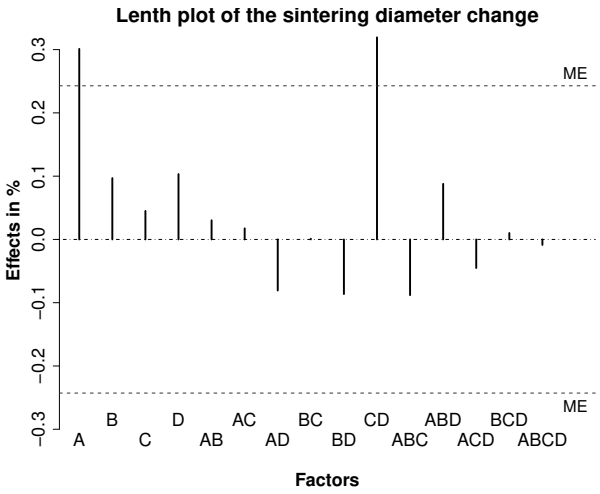

Figure 3: The Lenth plot indicates a decreasing diameter change at the higher level of factor A and due to the interaction CD. The main effects C and D were not significant.

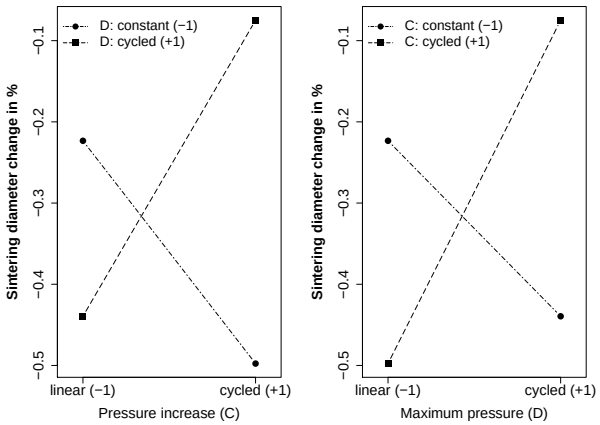

Figure 4: The interaction plot shows that the effect of one of the factors C and D on the sintering diameter change depended on the level of the other factor.

Table 4: Results with standard deviations for properties with multiple measurements (A: particle size distribution, B: maximum pressure, C: pressure increase (linear/cyclic), D: maximum pressure cycling (constant/cycled), $E_{0\mathrm{TS}}$ and $E_{1\mathrm{TS}}$: Young's modulus before and after thermal shock, respectively, $E_{1\mathrm{TS}}/E_{0\mathrm{TS}}$: remaining Young's modulus after one thermal shock). The run order is given for the fabrication of the samples. For each property measurement the samples were randomized.

Run	Order	Factors				Apparent porosity	Apparent density	Sintering diameter change	Median pore size	$E_{0\,\mathrm{TS}}$	$E_{1\,\mathrm{TS}}$	$E_{1\,\mathrm{TS}}/E_{0\,\mathrm{TS}}$
		A	B	C	D	(%)	(g/cm^3)	(μm)	(%)	(GPa)	(GPa)	(%)
1	7	−1	−1	−1	−1	17.78 ± 0.03	3.10 ± 0.00	−0.47 ± 0.38	3.24	48.16	25.29	52.51
2	8	+1	−1	−1	−1	19.22 ± 0.08	3.02 ± 0.00	−0.17 ± 0.24	4.40	29.96	14.17	47.31
3	9	−1	+1	−1	−1	16.80 ± 0.11	3.14 ± 0.00	−0.30 ± 0.16	3.03	40.47	19.75	48.80
4	10	+1	+1	−1	−1	18.42 ± 0.04	3.06 ± 0.00	0.04 ± 0.09	3.98	31.19	15.45	49.55
5	5	−1	−1	+1	−1	17.53 ± 0.14	3.11 ± 0.00	−0.88 ± 0.53	2.60	43.79	22.04	50.32
6	6	+1	−1	+1	−1	19.41 ± 0.08	3.02 ± 0.00	−0.29 ± 0.16	4.19	25.57	11.88	46.45
7	15	−1	+1	+1	−1	16.68 ± 0.09	3.15 ± 0.00	−0.56 ± 0.26	2.89	46.00	25.54	55.53
8	16	+1	+1	+1	−1	18.22 ± 0.07	3.06 ± 0.00	−0.26 ± 0.17	4.70	27.40	13.71	50.01
9	1	−1	−1	−1	+1	17.71 ± 0.16	3.11 ± 0.00	−0.46 ± 0.21	2.41	41.99	22.71	54.08
10	2	+1	−1	−1	+1	19.41 ± 0.10	3.02 ± 0.00	−0.42 ± 0.22	4.24	27.40	12.09	44.13
11	3	−1	+1	−1	+1	16.92 ± 0.11	3.14 ± 0.00	−0.67 ± 0.14	2.36	45.11	22.44	49.74
12	4	+1	+1	−1	+1	18.33 ± 0.09	3.06 ± 0.00	−0.21 ± 0.34	4.31	31.83	15.11	47.48
13	13	−1	−1	+1	+1	17.44 ± 0.03	3.12 ± 0.00	−0.17 ± 0.20	2.67	45.12	24.12	53.45
14	14	+1	−1	+1	+1	19.19 ± 0.14	3.03 ± 0.01	0.00 ± 0.14	3.84	31.07	15.25	49.07
15	11	−1	+1	+1	+1	16.82 ± 0.19	3.14 ± 0.01	−0.17 ± 0.14	2.97	45.95	21.14	46.00
16	12	+1	+1	+1	+1	18.21 ± 0.14	3.06 ± 0.01	0.04 ± 0.16	3.67	30.36	15.07	49.65

Table 5: ANOVA with p-values of the factorial experimental design on the investigated responses with multiple measurements (apparent porosity and apparent density measured by Archimedes' method, sintering shrinkage determined by measuring the diameter of the cylinders before and after firing). A: particle size distribution, B: maximum pressure, C: pressure increase, D: maximum pressure cycling, E: thermal shock (TS), A:B ... D:E: interaction effects, level of significance: $p < 0.05$, only two factor interactions were taken into account.

Effect	Sintering diameter change	Apparent porosity	Apparent density	Median pore diameter	Young's modulus (E)	$E_{1\,\mathrm{TS}}/E_{0\,\mathrm{TS}}$
A	$9.08 \cdot 10^{-06}$	$< 2 \cdot 10^{-16}$	$< 2 \cdot 10^{-16}$	$1.00 \cdot 10^{-03}$	$5.69 \cdot 10^{-11}$	0.08
B	0.12	$< 2 \cdot 10^{-16}$	$< 2 \cdot 10^{-16}$	0.84	0.64	0.97
C	0.47	$1.23 \cdot 10^{-04}$	$6.28 \cdot 10^{-05}$	0.80	0.94	0.60
D	0.10	0.95	0.82	0.18	0.62	0.60
A:B	0.62	$3.23 \cdot 10^{-03}$	0.01	0.84	0.14	0.17
A:C	0.78	0.15	0.16	0.72	0.26	0.62
A:D	0.19	0.44	0.49	0.94	0.38	0.94
B:C	0.99	0.95	0.98	0.39	0.60	0.74
B:D	0.16	0.22	0.20	0.99	0.50	0.28
C:D	$3.16 \cdot 10^{-06}$	0.20	0.14	0.97	0.17	0.91
E	–	–	–	–	$7.65 \cdot 10^{-14}$	–
A:E	–	–	–	–	$8.31 \cdot 10^{-04}$	–
B:E	–	–	–	–	0.72	–
C:E	–	–	–	–	0.84	–
D:E	–	–	–	–	0.63	–

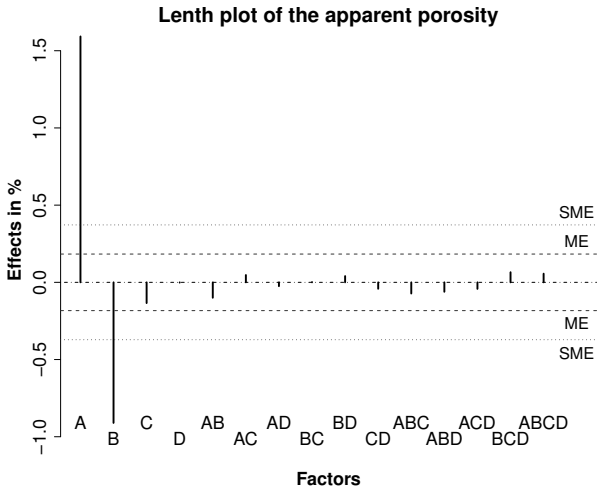

Figure 5: The Lenth plot of the apparent porosity shows a highly significant effect of the particle size distribution (A) and of the pressing pressure (B).

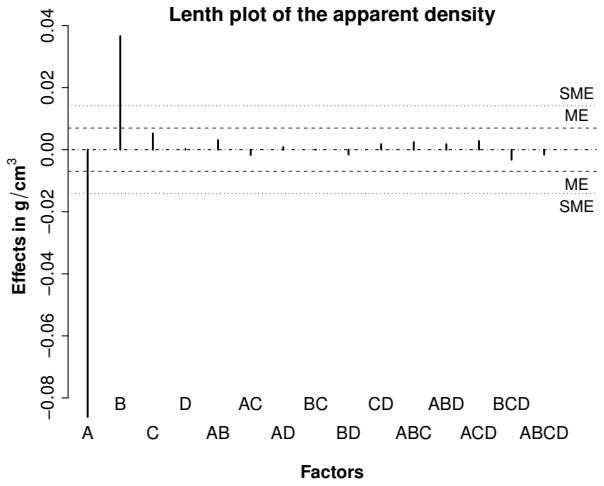

Figure 6: Similar but inverse effects as for the apparent porosity were observed for the apparent density, see Fig. 5.

inverse regarding the apparent porosity and the apparent density.

The effect of the factor A means that a lower distribution modulus n_{min} resulted in a lower apparent porosity. This can be most likely linked to an improved particle packing, which is in line with recent results of Fruhstorfer and Aneziris [38]. A lower apparent porosity due to a higher pressing pressure (factor B, level +1) was also expected due to a higher compaction [39].

Although the effect of the cycling during pressure increase was smaller (factor C, level +1), it was still statistically significant according to the ANOVA. Yet, while ANOVA only indicates statistical significance, the Lenth plots in Figs. 5 and 6 also contain the effect estimates of the unreplicated factorial experimental design. The Lenth plots also provide the margin of error (ME) and the simultaneous margin of error (SME) at a significance level $\alpha = 0.05$ to distinguish active from inactive effects. Consequently Lenth plots are very useful to estimate not only statistical significance of effects but also the effect size, which are equally important for a meaningful statistical analysis [40, 41]. Thus, there is evidence from the ANOVA that the effects C and AB are statistically significant regarding the apparent porosity and density, yet their effect sizes are apparently quite small.

A first possible reason for the statistically significant albeit small effect of factor C might be an improved particle rearrangement and movement of the particles due to a cycled pressure increase. Such rearrangement and movement is especially pronounced at the beginning of the compaction [42].

However, the non-significance of the cycling at maximum pressure (factor D) regarding the apparent density and porosity is inconsistent with previously reported results for fine grained ceramics. For example, Michaeli et al. [10] reported a positive effect of a pressure cycling at maximum pressure for alumina granules, while no effect was reported for a cycled pressure increase. Furthermore, Matsuo et al. [18] also reported an improved compaction due to a cycling at maximum pressure even for only ten cycles using submicron SiC powder, while a cycled pressure increase was not investigated.

The high density of refractories mainly derives from an optimized particle packing, while for fine grained ceramics sintering is much more important to obtain a high density [37, 43]. As a case in point, in the present study the linear sintering shrinkage and thus the linear densification during sintering was less than 1% for all samples. On the other hand, in a study by Yasuda et al. [19] the relative green density for fine grained SiO_2 ceramics was about 0.51 without cycling and 0.57 after 1000 cycles. Meanwhile, the average particle coordination number increased from about 6.5 without cycling to 7 after 1000 cycles [19]. The results of Yasuda et al. [19] also imply that it becomes exceedingly difficult to achieve higher densities, the higher number of pressure cycles. In the present study a very broad particle size distribution was applied, which is associated with a high particle coordination number and packing density [23, 44]. Due to the higher coordination number and the small residual porosity it can be assumed that it is difficult to achieve a higher density by cycling at maximum

pressure because the ceramic bodies are already highly compacted and thus the friction between the particles is too high to achieve particle rearrangement.

Moreover, Nishimura et al. [9] demonstrated that the higher the amplitude of the pressure as a function of the maximum pressure, the higher the achieved densification. In case of the present study, the amplitude was always 25 MPa and therefore relatively higher during a cycling at an increasing pressure (factor C) than at maximum pressure (D). Thus, the relatively higher pressure amplitude during the pressure increase might be a second contributing factor for the significant albeit small effect of the cycling during pressure increase on the apparent density and porosity. In addition, during the cycled pressure increase each pressure stage was higher than the previous one, which can also contribute to particle rearrangement.

Finally, the dimensions of the samples in this study were much larger than in all previous studies on fine grained ceramics. During cold isostatic pressing a radial stress distribution is present resulting in a higher pressure at the surface than in the center of the ceramic body [45]. Furthermore, the cycling frequency was quite low which is also associated with a somewhat lower compaction [15]. Although these factors were beyond the scope of this study, future work should investigate the influence of the pressure amplitude and cycling frequency as a function of the maximum pressure, pressure increase and particle packing.

3.4. Median pore size

With a lower particle size distribution modulus n_{min} and thus with a higher amount of the finest particle fraction (factor A, level −1), the median pore size was significantly smaller, as can be seen from the Lenth plot in Fig. 7 and from the ANOVA in Table 5. Furthermore, according to the Lenth plot in Fig. 7, the cycling at maximum pressure (factor D) was possibly (> ME) active whereas the three-way interaction ACD was probably active (> SME). The smaller median pore size with a wider particle size distribution (lower n_{min}) was most likely associated with a better particle packing, a higher particle coordination number as well as a higher number of microcracks. On the other hand, a wider particle size distribution and a higher amount of fines did not cause a coarsening of the pores, which was considered for high-alumina castables with a higher amount of calcined alumina [46].

The three-way interaction ACD on the median pore size is illustrated in Fig. 8. According to this interaction plot, the median pore size depended much on the interaction CD (cyclic pressure increase and cycling at maximum pressure). Additionally this interaction was reverse. Whereas for a low distribution modulus n_{min} the median pore size was lower when cycling occurred either during the pressure increase or at maximum pressure, the median pore size was lower at the high level of n_{min} if cycling was applied in the same run during pressure increase (factor C, level +1) and at maximum pressure (factor D, level +1). This implies that possibly the effect of pressure cycling on the pore size distribution and thus microstructure depends to some extent on the packing density and particle size.

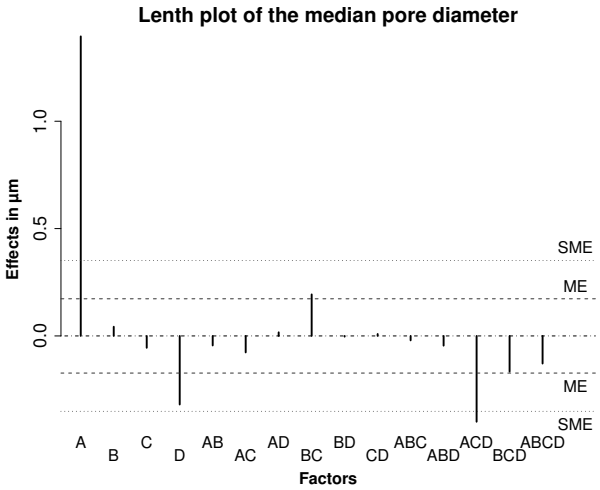

Figure 7: The Lenth plot of the median pore size indicates a high activity of the factors A (particle size distribution modulus) and the interaction ACD, while the factors D (pressure cycling at maximum pressure) and the interaction BC were possibly active.

3.5. Young's modulus before and after thermal shock

As evident from Table 4 and the Lenth plot in Fig. 9, a lower particle size distribution modulus n_{min} (factor A, level −1) significantly increased the Young's modulus, while the higher level of the distribution modulus n_{min} acted conversely. The higher Young's modulus can be mainly explained by the higher sintering activity of the particle size distribution containing a higher amount of fine particles and by an improved particle packing associated with a higher particle coordination number as was shown for the apparent density. These factors were also recently related to the cold crushing strength of alumina refractories as a function of the particle size distribution modulus n_{min} [38]. Furthermore, Fruhstorfer and Aneziris [38] also correlated the cold crushing strength with the apparent density. Yet, remarkably, a higher pressing pressure (factor B) which resulted in a higher apparent density did not yield a statistically significantly different Young's modulus, see Fig. 6 and Fig. 9.

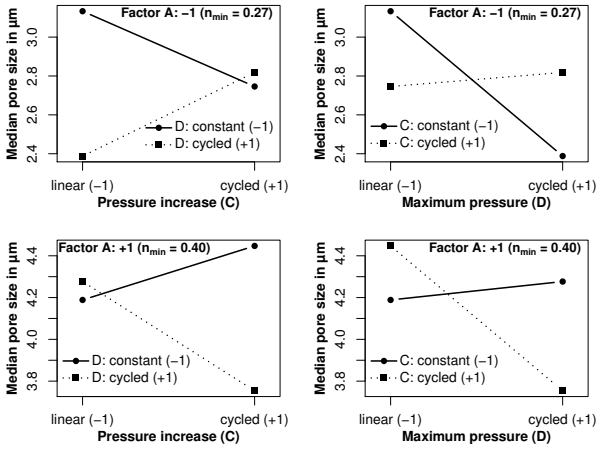

Figure 8: The interaction plots of the interaction ACD on the median pore size indicate that the median pore size depended significantly on the levels of the pressure cycling during pressure increase (factor C) and at maximum pressure (factor D). The effect was reverse depending on the level of the particle size distribution modulus (factor A).

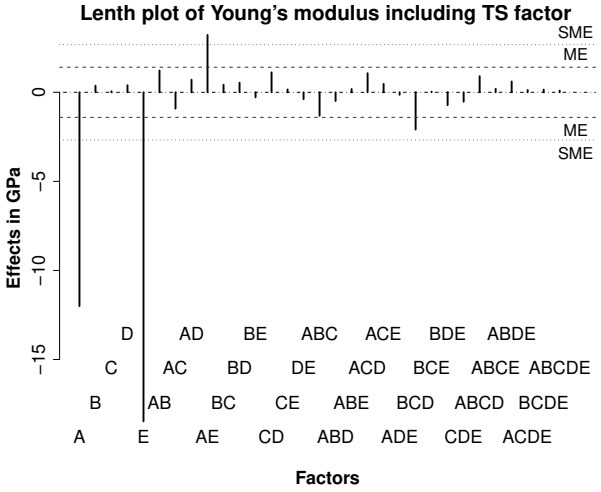

Figure 9: The Lenth plot reveals a significant effect of the particle size distribution modulus (factor A), thermal shock treatment (factor E) and their interaction (AE) on the Young's modulus.

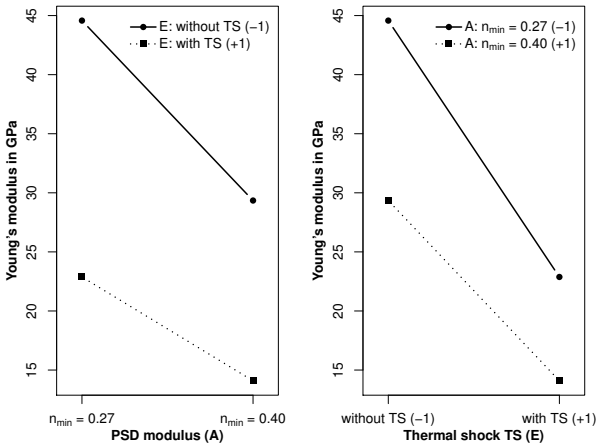

Figure 10: The interaction effect shows that the Young's modulus before as well as after thermal shock was higher for a low distribution modulus n_{min} (level −1, factor A). The absolute decrease due to thermal shock was somewhat higher for a lower level of n_{min}, while no statistical significant difference of the relative change was determined (see Fig. 11).

Secondly, not only the particle size distribution modulus n_{min} (factor A) but also the thermal shock treatment (factor E) and their interaction AE had a significant effect on the Young's modulus, cf. Fig. 9. The lower Young's modulus after thermal shock is a general characteristic of ceramic materials such as refractories. Additionally the interaction AE, which is illustrated in Fig. 10, also indicates that a higher absolute Young's modulus before thermal shock resulting from an improved particle packing and stronger sintering resulted in a somewhat higher absolute drop in the Young's modulus after thermal shock. But the interaction plot in Fig. 10 also shows that even after thermal shock the compositions with a higher Young's modulus before thermal shock retained a higher Young's modulus after thermal shock, which is in good agreement with results from Schafföner et al. [47]. On the other hand, the particle size distribution as well as all other investigated factor were non-significant regarding the relative drop of the Young's modulus after thermal shock, cf. Fig. 11. Again a similar behavior was recently observed for $CaZrO_3$ refractories by Schafföner et al. [47].

Numerous models have been developed to correlate mechanical properties including the strength and the Young's modulus of refractories and other coarse grained materials such as concrete with their porosity or pore size. Table 6 lists several of these models together with their Pearson correlation coefficients for the Young's modulus before thermal shock. Even the early

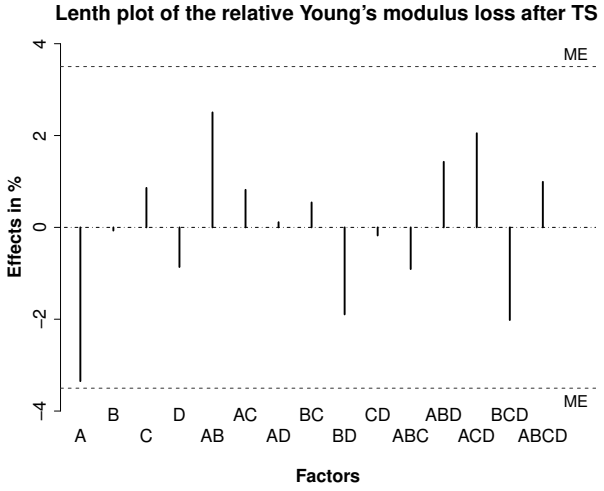

Figure 11: No factor was statistically active regarding the relative change of the Young's modulus due to thermal shock. However, the relative change was slightly smaller for the lower level of factor A (n_{min} = 0.27) indicating that an improved particle packing not only resulted in a higher absolute Young's modulus before and after thermal shock but also in a sightly smaller drop due to thermal shock, which should investigated in more detail in further studies.

model proposed by Hasselman [48] assuming a linear dependency of the Young's modulus from the apparent porosity had a correlation coefficient of 0.85. Furthermore, the calculated values for E_0 and K are in excellent agreement with comparable values for alumina given by Hasselman [48]. The highest correlation coefficient was obtained for the adapted model of Kumar and Bhattacharjee [49]. Originally this model was proposed for the compressive strength of concrete, while in the present study it was used to correlate the Young's modulus. As the only reviewed model it takes the porosity together with the pore size and possibly microcracks into account. The other models assuming non-linear relationships between the Young's modulus and either the apparent porosity or the median pore size did not result in significantly improved correlation coefficients compared to the model of Hasselman [48]. Most interesting is also that the last model correlating the Young's modulus with the median pore size only has a similar correlation coefficient as the models assuming a correlation with the apparent porosity. This can be attributed to the particle size distribution and the resulting particle packing which significantly influenced the apparent porosity as well as the median pore size.

The findings of this study regarding the Young's modulus before and after thermal shock compare well with previous studies. First, for comparable ceramics including refractories the ones with a higher Young's modulus generally exhibit a higher absolute drop in Young's modulus due to thermal shock, if crack initiation cannot be avoided [47, 54, 55]. Yet, refractories with a higher original Young's modulus often also have a higher Young's modulus after thermal shock. Thus, the relation between the Young's modulus before thermal shock and its relative change due to thermal shock is often less evident than for the absolute change [22, 47, 54], which was also the case in the present study. Generally high mechanical properties after thermal shock are most important and the aim for the development of refractories is thus to optimize mechanical properties before thermal shock accordingly. Therefore, in comparison refractories with a higher Young's modulus and strength after thermal shock should be usually preferred to refractories with a lower relative change of mechanical properties due to thermal shock [56].

Secondly, a lower porosity as well as a smaller pore size are generally assumed to have an increasing effect on the Young's modulus and the strength [49]. If crack initiation due to thermal shock cannot be avoided, ceramics should have a high thermal shock damage resistance. To achieve a high thermal shock damage resistance, refractories with a high Young's modulus and a low strength are often most beneficial [56]. A higher porosity has a reducing effect on the thermal shock fracture resistance because it lowers the strain at fracture [57–59]. However, while some studies revealed an improvement of the thermal shock damage resistance [60, 61], no effect or even a slightly worse thermal shock damage resistance in terms of retained mechanical properties was reported by others [47, 59, 62]. By contrary, several studies indicate an improvement of the thermal shock damage resistance with a decreasing pore size [53, 61]. Hasselman [48] concluded that a decreasing pore size at a given porosity results in a higher number of propagating cracks in case of thermal shock and in a higher number of elastic discontinuities arresting or deflecting cracks. Both factors contribute to a shorter distance that cracks can propagate [56, 60].

Third, as this study shows the model proposed by Fruhstorfer and Aneziris [23] seems to be particularly useful to design particle size distributions for refractories with a high packing density resulting in smaller pores as well as in a higher microcrack density [44]. Correspondingly the smaller pores are associated with a higher Young's modulus before and after thermal shock and even improved its relative decrease to some extent. This result also strengthens the theory that small pores also act as microcracks which generally improve the thermal shock damage resistance [48, 63–65]. On the other hand, the results also indicate that process-

Table 6: Models to correlating the Young's modulus before thermal shock with the apparent porosity (P) and median pore radius (r_m), whereas r is the correlation coefficient according to Pearson. E_0 is the calculated Young's modulus at zero porosity, which was much higher than the actual Young's modulus of pure alumina (309 GPa [50]).

Model	Factor estimates	r	Reference
$E = E_0(1 - aP)$	$E_0 = 168.72\,\text{GPa}$, $a = 4.34$	0.85	Hasselman [48]
$E = K(1 - P)/\sqrt{r_m}$	$K = 58.67\,\text{GPa} \cdot \mu\text{m}^{0.5}$	0.88	adapted from Kumar and Bhattacharjee [49], this work
$E = E_0(1 - aP)^n$	$E_0 = 170.10\,\text{GPa}$, $a = 4.33$, $n = 1.01$	0.85	Phani and Niyogi [51]
$E = E_0 \exp(-bP)$	$E_0 = 1291.79\,\text{GPa}$, $b = 19.83$	0.85	Spriggs [52]
$E = K/r_m^c$	$K = 55.22\,\text{GPa} \cdot \mu\text{m}^c$, $c = 0.79$	0.86	adapted from Li et al. [53], this work

ing strategies that only result in a higher density but are less effective to increase the Young's modulus and the number of pores and microcracks such as a higher pressing pressure are much less effective to improve the thermal shock damage resistance of refractories. Moreover, to investigate the thermal shock damage resistance as a function of porosity, the pore size should be also taken into account because often a higher porosity is accompanied with larger pores causing opposing effects on the Young's modulus and the thermal shock damage resistance [47]. Due to the promising results of this study, tailoring the pore size distribution of refractories to improve thermomechanical properties by advanced processing will be further investigated in future studies.

4. Conclusions

The present study investigated the cyclic cold isostatic pressing of coarse grained oxide ceramics using a 2^4 full factorial experimental design. The cycling of the pressure was applied during the pressure increase as well as at maximum pressure. Additionally the study evaluated the effects of the maximum pressure and the particle size distribution on the physical, mechanical and thermomechanical properties.

In contrast to fine grained ceramics only a minor effect on the apparent density and apparent porosity was observed during a cyclic pressure increase. Secondly, a cycling at maximum pressure reduced the median pore size to some extent.

The study validated the usefulness of the particle size distribution model of Fruhstorfer and Aneziris [23] to achieve a high packing density of refractories resulting in a higher apparent density and apparent porosity, respectively. In addition the median pore size was significantly reduced. The lower pore size resulted in a higher Young's modulus before and after thermal shock and also contributed to a slightly smaller relative drop of the Young's modulus due to thermal shock. This result shows that a higher particle coordination in refractories leads to smaller pores and particularly to a higher number of pores. This higher number of pores then act as points of crack initiation and crack arrest and deflection in case of thermal shock limiting the crack propagation of individual cracks. Eventually that leads to improved thermal shock damage resistance and is in excellent agreement with the predictions of Hasselman [48]. Thus, the tailoring of the pore size distribution of refractories offers much promise to improve mechanical and thermomechanical properties.

Acknowledgment

The authors would like to thank the German Research Foundation (DFG) for supporting this project under grant number AN 322/32-1. Furthermore, the authors thank Rico Kaulfürst for the cold isostatic pressing experiments, Ursula Querner for the mercury intrusion porosimetry analyses as well as Christina Faßauer and Miriam Bach for the help with the experiments.

[1] R. J. Henderson, H. W. Chandler, A. R. Akisanya, H. Barber, B. Moriarty, Finite element modelling of cold isostatic pressing, Journal of the European Ceramic Society 20 (8) (2000) 1121–1128, doi:10.1016/S0955-2219(99)00280-0.

[2] H. C. Yang, J. K. Kim, K. T. Kim, Rubber isostatic pressing and cold isostatic pressing of metal powder, Materials Science and Engineering: A 382 (1-2) (2004) 41–49, doi:10.1016/j.msea.2004.04.056.

[3] Y. Gu, R. J. Henderson, H. W. Chandler, Visualizing isostatic pressing of ceramic powders using finite element analysis, Journal of the European Ceramic Society 26 (12) (2006) 2265–2272, doi:10.1016/j.jeurceramsoc.2005.03.256.

[4] H. C. Weerasinghe, P. M. Sirimanne, G. P. Simon, Y.-B. Cheng, Cold isostatic pressing technique for producing highly efficient flexible dye-sensitised solar cells on plastic substrates, Progress in Photovoltaics: Research and Applications 20 (3) (2012) 321–332, doi:10.1002/pip.1140.

[5] J. Shao, F. Liu, W. Dong, R. Tao, Z. Deng, X. Fang, S. Dai, Low temperature preparation of TiO_2 films by cold isostatic pressing for flexible dye-sensitized solar cells, Materials Letters 68 (2012) 493–496, doi:10.1016/j.matlet.2011.11.040.

[6] R. Henderson, H. Chandler, A. Akisanya, B. Moriarty, Bag design in isostatic pressing, Materials & Design 21 (4) (2000) 259–262, doi:10.1016/S0261-3069(99)00076-X.

[7] S. Lee, K. Kim, A densification model for powder materials under cold isostatic pressing—Effect of adhesion and friction of

rubber molds, Materials Science and Engineering: A 498 (12) (2008) 359–368, doi:10.1016/j.msea.2008.08.020.

[8] Y. Fu, Z. Tao, X. Hou, Weibull distribution of the fracture strength of 99% alumina ceramic reshaped by cold isostatic pressing, Ceramics International 40 (6) (2014) 7661–7667, doi:10.1016/j.ceramint.2013.12.053.

[9] T. Nishimura, K. Jinbo, Y. Matsuo, S. Kimura, Forming of ceramic powders by cyclic-CIP: effect of bias pressure, Nippon Seramikkusu Kyokai Gakujutsu Ronbunshi 98 (7) (1990) 735–738.

[10] N. Michaeli, C. Aneziris, H. Maier, Cycling pressure during cold isostatic pressing, in: H. Hausner, G. L. Messing, S. Hirano (Eds.), Ceramic Processing Science and Technology, vol. 51 of *Ceramic Transactions*, 277–281, 1994.

[11] C.-Y. Huang, G. S. Daehn, Densification of composite powder compacts in pressure cycling, Acta Materialia 44 (3) (1996) 1035–1045, doi:10.1016/1359-6454(95)00230-8.

[12] G. Jiang, W. Wu, G. Daehn, R. Wagoner, Experimental and numerical investigation of idealized consolidation: Part II: Cyclic compaction, Acta Materialia 48 (17) (2000) 4331–4335, doi:10.1016/S1359-6454(00)00207-X.

[13] G. Jiang, G. Daehn, J. Lannutti, Y. Fu, R. Wagoner, Effects of lubrication and aspect ratio on the consolidation of metal matrix composites under cyclic pressure, Acta Materialia 49 (8) (2001) 1471–1477, doi:10.1016/S1359-6454(01)00026-X.

[14] G. Jiang, G. S. Daehn, R. H. Wagoner, Observations on densification of Al-Al_2O_3 composite powder compacts by pressure cycling, Powder Metallurgy 46 (1) (2003) 78–82, doi:10.1179/003258903225010505.

[15] A. Zavaliangos, A. Laptev, The densification of powder mixtures containing soft and hard components under static and cyclic pressure, Acta Materialia 48 (10) (2000) 2565–2570, doi:10.1016/S1359-6454(00)00066-5.

[16] Y. Fu, G. Jiang, J. Lannutti, R. Wagoner, G. Daehn, Effect of cyclic pressure consolidation on the uniformity of metal matrix composites, Metallurgical and Materials Transactions A 33 (1) (2002) 183–191, doi:10.1007/s11661-002-0017-5.

[17] A. Tavakoli, A. Simchi, S. S. Reihani, Study of the compaction behavior of composite powders under monotonic and cyclic loading, Composites Science and Technology 65 (14) (2005) 2094–2104, doi:10.1016/j.compscitech.2005.05.016.

[18] Y. Matsuo, T. Nishimura, K. Yasuda, K. Jinbo, S. Kimura, Forming of silicon carbide powder by cyclic CIP, Nippon seramikkusu kyokai gakujutsu ronbunshi 99 (3) (1991) 187–190.

[19] K. Yasuda, F. Takase, Y. Matsuo, Stochastic analysis on coordination number distribution of particles during powder compaction, Advanced Powder Technology 24 (5) (2013) 871–878, doi:10.1016/j.apt.2013.05.002.

[20] G. Jiang, G. S. Daehn, R. Wagoner, Void filling and cluster breaking of metal-ceramic composites under pressure cycling, Scripta Materialia 44 (2) (2001) 287–292, doi:10.1016/S1359-6462(00)00579-0.

[21] G. Jiang, G. S. Daehn, R. Wagoner, Inclusion particle size effects on the cyclic compaction of powder composites, Scripta Materialia 44 (7) (2001) 1117–1123, doi:10.1016/S1359-6462(01)00659-5.

[22] S. Schafföner, C. Dietze, S. Möhmel, J. Fruhstorfer, C. G. Aneziris, Refractories containing fused and sintered alumina aggregates: Investigations on processing, particle size distribution and particle morphology, Ceramics International 43 (5) (2017) 4252–4262, doi:10.1016/j.ceramint.2016.12.067.

[23] J. Fruhstorfer, C. G. Aneziris, The Influence of the Coarse Fraction on the Porosity of Refractory Castables, Journal of Ceramic Science and Technology 5 (2) (2014) 155–165.

[24] J. Fruhstorfer, S. Barlag, M. Thalheim, L. Schöttler, C. G. Aneziris, Upright die pressing of refractory hollowware for steel ingot casting with reduced clay content, Ceramics International 42 (2, Part B) (2016) 3219–3228, doi:10.1016/j.ceramint.2015.10.111.

[25] S. Schafföner, C. G. Aneziris, H. Berek, J. Hubálková, A. Priese, Fused calcium zirconate for refractory applications, Journal of the European Ceramic Society 33 (15–16) (2013) 3411–3418.

[26] M. Asmani, C. Kermel, A. Leriche, M. Ourak, Influence of porosity on Young's modulus and Poisson's ratio in alumina ceramics, Journal of the European Ceramic Society 21 (8) (2001) 1081–1086, doi:10.1016/S0955-2219(00)00314-9.

[27] R. V. Lenth, Quick and Easy Analysis of Unreplicated Factorials, Technometrics 31 (4) (1989) 469–473, doi:10.1080/00401706.1989.10488595.

[28] M. J. Crawley, Statistics: An Introduction using R, Wiley John & Sons, 2nd edn., doi:10.1002/9781119941750, 2014.

[29] N. Brachhold, S. Schafföner, C. G. Aneziris, Investigation of alkali corrosion resistance of potassium aluminosilicates using statistical techniques, Ceramics International 41 (1, Part B) (2015) 1447–1456.

[30] D. C. Montgomery, Design and analysis of experiments, John Wiley & Sons, 2008.

[31] M. Hamada, N. Balakrishnan, Analyzing unreplicated factorial experiments: A review with some new proposals, Statistica Sinica 8 (1998) 1–41.

[32] J. Lawson, Design and Analysis of Experiments with R, CRC Press, 2014.

[33] C. F. J. Wu, M. S. Hamada, Experiments: planning, analysis, and optimization, John Wiley & Sons, 2009.

[34] R Core Team, R: A Language and Environment for Statistical Computing, R Foundation for Statistical Computing, Vienna, Austria, 2017.

[35] J. S. Reed, Principles of Ceramic Processing, Wiley & Sons, 2 edn., 1995.

[36] R. German, Sintering densification for powder mixtures of varying distribution widths, Acta Metallurgica et Materialia 40 (9) (1992) 2085–2089, doi:10.1016/0956-7151(92)90125-X.

[37] R. German, Prediction of sintered density for bimodal powder mixtures, Metallurgical Transactions A 23 (5) (1992) 1455–1465.

[38] J. Fruhstorfer, C. G. Aneziris, Influence of particle size distributions on the density and density gradients in uniaxial compacts, Ceramics International 43 (16) (2017) 13175–13184, doi:10.1016/j.ceramint.2017.07.011.

[39] R. W. Heckel, Density-pressure relationships in powder compaction, Transactions of the Metallurgical Society of AIME 221 (4) (1961) 671–675.

[40] D. Lakens, Calculating and reporting effect sizes to facilitate cumulative science: a practical primer for t-tests and ANOVAs, Frontiers in Psychology 4 (2013) 863, doi:10.3389/fpsyg.2013.00863.

[41] C. O. Fritz, P. E. Morris, J. J. Richler, Effect size estimates: Current use, calculations, and interpretation., Journal of Experimental Psychology: General 141 (1) (2012) 2–18, doi:10.1037/a0024338.

[42] R. Carneim, G. Messing, Response of granular powders to uniaxial loading and unloading, Powder technology 115 (2) (2001) 131–138.

[43] R. M. German, Powder Metallurgy & Particulate Materials Processing, vol. 105, Metal powder industries federation Princeton, NJ, 2005.

[44] J. Fruhstorfer, C. Demuth, P. Goetze, C. G. Aneziris, S. Ray, U. Gross, D. Trimis, How the coarse fraction influences the microstructure and the effective thermal conductivity of alu-

mina castables - An experimental and numerical study, Journal of the European Ceramic Society 38 (1) (2018) 303–312, doi:10.1016/j.jeurceramsoc.2017.07.038.

[45] K. Yasuda, S. Tanaka, M. Naito, Stochastic analysis on ceramic granule collapse in powder compact during cold isostatic pressing, Advanced Powder Technology 27 (3) (2016) 940–947, doi:10.1016/j.apt.2016.02.032.

[46] A. Studart, R. Pileggi, V. Pandolfelli, J. Gallo, High-alumina multifunctional refractory castables, American Ceramic Society Bulletin 80 (11) (2001) 34–40.

[47] S. Schafföner, J. Fruhstorfer, C. Faßauer, L. Freitag, C. Jahn, C. G. Aneziris, Influence of in situ phase formation on properties of calcium zirconate refractories, Journal of the European Ceramic Society 37 (1) (2017) 305–313, doi:10.1016/j.jeurceramsoc.2016.08.017.

[48] D. P. H. Hasselman, Relation Between Effects of Porosity on Strength and on Young's Modulus of Elasticity of Polycrystalline Materials, Journal of the American Ceramic Society 46 (11) (1963) 564–565, doi:10.1111/j.1151-2916.1963.tb14615.x.

[49] R. Kumar, B. Bhattacharjee, Porosity, pore size distribution and in situ strength of concrete, Cement and Concrete Research 33 (1) (2003) 155–164, doi:10.1016/S0008-8846(02)00942-0.

[50] J. Wachtman, D. G. Lam, Young's Modulus of Various Refractory Materials as a Function of Temperature, Journal of the American Ceramic Society 42 (5) (1959) 254–260, doi:10.1111/j.1151-2916.1959.tb15462.x.

[51] K. Phani, S. Niyogi, Young's modulus of porous brittle solids, Journal of Materials Science 22 (1) (1987) 257–263, doi:10.1007/BF01160581.

[52] R. M. Spriggs, Expression for Effect of Porosity on Elastic Modulus of Polycrystalline Refractory Materials, Particularly Aluminum Oxide, Journal of the American Ceramic Society 44 (12) (1961) 628–629, doi:10.1111/j.1151-2916.1961.tb11671.x.

[53] Y. Li, X. Li, B. Zhu, P. Chen, The relationship between the pore size distribution and the thermo-mechanical properties of high alumina refractory castables, International Journal of Materials Research 107 (3) (2016) 263–268, doi:10.3139/146.111336.

[54] D. Larson, J. Coppola, D. Hasselman, R. Bradt, Fracture Toughness and Spalling Behavior of High-Al_2O_3 Refractories, Journal of the American Ceramic Society 57 (10) (1974) 417–421, doi:10.1111/j.1151-2916.1974.tb11372.x.

[55] D. Hasselman, Strength Behavior of Polycrystalline Alumina Subjected to Thermal Shock, Journal of the American Ceramic Society 53 (9) (1970) 490–495, doi:10.1111/j.1151-2916.1970.tb15997.x.

[56] D. Hasselman, Elastic Energy at Fracture and Surface Energy as Design Criteria for Thermal Shock, Journal of the American Ceramic Society 46 (11) (1963) 535–540, doi:10.1111/j.1151-2916.1963.tb14605.x.

[57] R. Coble, W. Kingery, Effect of Porosity on Thermal Stress Fracture, Journal of the American Ceramic Society 38 (1) (1955) 33–37, doi:10.1111/j.1151-2916.1955.tb14549.x.

[58] R. Coble, W. Kingery, Effect of Porosity on Physical Properties of Sintered Alumina, Journal of the American Ceramic Society 39 (11) (1956) 377–385, doi:10.1111/j.1151-2916.1956.tb15608.x.

[59] Y. Shao, R. Du, X. Wu, F. Song, X. Xu, C. Jiang, Effect of porosity on the crack pattern and residual strength of ceramics after quenching, Journal of Materials Science 48 (18) (2013) 6431–6436, doi:10.1007/s10853-013-7444-0.

[60] J. She, J. Yang, T. Ohji, Thermal shock resistance of porous silicon nitride ceramics, Journal of Materials Science Letters 22 (5) (2003) 331–333, doi:10.1023/A:1022678606160.

[61] X. Jin, L. Dong, H. Xu, L. Liu, N. Li, X. Zhang, J. Han, Effects of porosity and pore size on mechanical and thermal properties as well as thermal shock fracture resistance of porous ZrB_2-SiC ceramics, Ceramics International 42 (7) (2016) 9051–9057, doi:10.1016/j.ceramint.2016.02.164.

[62] J. Fruhstorfer, S. Schafföner, J. Werner, T. Wetzig, L. Schöttler, C. G. Aneziris, Thermal Shock Performance of Refractories for Application in Steel Ingot Casting, Journal of Ceramic Science and Technology 7 (2) (2016) 173–182, doi:10.4416/JCST2016-00010.

[63] S. Schafföner, C. G. Aneziris, Pressure slip casting of coarse grain oxide ceramics, Ceramics International 38 (1) (2012) 417–422, doi:10.1016/j.ceramint.2011.06.064.

[64] D. Hasselman, Unified Theory of Thermal Shock Fracture Initiation and Crack Propagation in Brittle Ceramics, Journal of the American Ceramic Society 52 (11) (1969) 600–604, doi:10.1111/j.1151-2916.1969.tb15848.x.

[65] V. R. Salvini, V. C. Pandolfelli, R. C. Bradt, Extension of Hasselman's thermal shock theory for crack/microstructure interactions in refractories, Ceramics International 38 (7) (2012) 5369–5375, doi:10.1016/j.ceramint.2012.03.046.